ELSEVIER

Journal of Nuclear Materials 251 (1997) 157–171

journal of nuclear materials

A computational microscopy study of nanostructural evolution in irradiated pressure vessel steels

G.R. Odette *, B.D. Wirth

Department of Mechanical and Environmental Engineering, University of California Santa Barbara, Santa Barbara, CA 91106, USA

Abstract

Nanostructural features that form in reactor pressure vessel steels under neutron irradiation at around 300°C lead to significant hardening and embrittlement. Continuum thermodynamic-kinetic based rate theories have been very successful in modeling the general characteristics of the copper and manganese nickel rich precipitate evolution, often the dominant source of embrittlement. However, a more detailed atomic scale understanding of these features is needed to interpret experimental measurements and better underpin predictive embrittlement models. Further, other embrittling features, believed to be subnanometer defect (vacancy)–solute complexes and small regions of modest enrichment of solutes are not well understood. A general approach to modeling embrittlement nanostructures, based on the concept of a computational microscope, is described. The objective of the computational microscope is to self-consistently integrate atomic scale simulations with other sources of information, including a wide range of experiments. In this work, lattice Monte Carlo (LMC) simulations are used to resolve the chemically and structurally complex nature of Cu–Mn–Ni–Si precipitates. The LMC simulations unify various nanoscale analytical characterization methods and basic thermodynamics. The LMC simulations also reveal that significant coupled vacancy and solute clustering takes place during cascade aging. The cascade clustering produces the metastable vacancy–cluster solute complexes that mediate flux effects. Cascade solute clustering may also play a role in the formation of dilute atmospheres of solute enrichment and enhance the nucleation of manganese–nickel rich precipitates at low Cu levels. Further, the simulations suggest that complex, highly correlated processes (e.g. cluster diffusion, formation of favored vacancy diffusion paths and solute scavenging vacancy cluster complexes) may lead to anomalous fast thermal aging kinetics at temperatures below about 450°C. The potential technical significance of these phenomena is described. © 1997 Elsevier Science B.V.

1. Introduction

Developing models to predict irradiation embrittlement of reactor pressure vessels (RPV) is a great challenge, in part because the relevant phenomena encompass an extraordinary range of length and time scales. Embrittlement is initiated by the production of primary damage in the form of vacancies and interstitials generated over time scales on-the-order of picoseconds and atomic length scales. At the other end of a long chain of events, the nanoscale features that evolve under irradiation can lead to severe degradation of the fracture resistance of massive pressure vessels containing more than 10^{31} atoms over time scales of a gigasecond.

Embrittlement is controlled by the synergistic action of a large number of irradiation variables [flux (ϕ), fluence (ϕt), irradiation temperature (T_i)] and metallurgical variables (composition, heat treatment and microstructure) [1–11]. For example: (a) increased ϕ can either increase, decrease or not influence embrittlement, depending on the specific combination of ϕ, T_i, ϕt and alloy Cu and Ni content; and (b) Ni enhances embrittlement by at least three mechanisms, including those that are both synergistic and independent of Cu. Hence, purely empirical approaches to correlating embrittlement data are subject to large uncertainties and cannot be relied upon for extrapolation.

* Corresponding author. Tel.: +1-805 893 3525; fax: +1-805 893 8651; e-mail: odette@engineering.ucsb.edu.

PII S0022-3115(97)00267-5

Indeed, physically based models, verified by independent measurements, have proven to be critical to developing robust engineering correlations of embrittlement and annealing data [11,12]. These models may also help to avoid unpleasant future technical surprises. Our approach to modeling such complex engineering phenomena includes carefully designed basic experiments with controlled changes in variables, or variable sets, as well as specific studies to resolve the underlying mechanisms. Integrated embrittlement models involve the following elements [13–18]: (a) the physics of defect production and defect properties; (b) the basic thermodynamics and kinetics governing the redistribution of alloy constituents and defects; (c) the structure–property relationships describing how the nanofeatures alter fundamental flow and local fracture properties; and (d) the micromechanics relating the flow and local fracture properties to macroscopic measures of toughness. Most fundamentally, reliable physical models require a good understanding of the nanoscale features, which will be the focus of this paper.

Most of the previous atomistic research has been on primary defect production in pure metals. Rate theory methods have been used to track the fate of the defects and model defect driven solute segregation. However, useful understanding of the features that form under irradiation requires models that also treat basic compositionally sensitive alloy thermodynamics and kinetics. This paper describes the current understanding of how fundamental thermodynamic and kinetic processes mediate nanostructural evolution in RPV steels, with emphasis on the role of atomic-scale mechanisms and displacement cascades. Linking of various length and time scales, as well as integrating various sources of information, is carried out using what we describe as a computational microscope, capable of near atomic scale resolution. While specifically addressing damage mechanisms in RPV steels, these approaches are clearly pertinent to many other radiation damage problems, including those encountered in fusion technology.

2. Overview of embrittlement processes and nanofeatures

Embrittlement is commonly characterized by increases in the Charpy-V-notch 41J transition temperature. RPVs operate at around 290 ± 30°C and experience end-of-life exposures of less than 0.08 displacements-per-atom (dpa) accumulated at rates less than 10^{-10} dpa/s [11]. These 'low dose' irradiation conditions have little or no effect on the coarse-scale bainitic and carbide microstructures that mediate the critical local stresses needed to trigger brittle cleavage in western RPV steels. Thus, transition temperature shifts are caused by the yield stress increases produced by high concentrations ($> 10^{23}/m^3$) of the nanoscale features that form under irradiation. These features include both well formed precipitates and so-called matrix features comprised of point defect clusters complexed with solutes and regions of solute enrichment that are not well formed precipitates. The terminology used to describe the various features and some of their key characteristics are described in Table 1.

Low alloy RPV steels (plates, forgings and welds) contain Mn (0.7–1.7%), Ni (0.2 to 1.4%), Mo ($\approx 0.5\%$), Si (0.25–0.5%) and, in the case of forgings, Cr (0.25–0.5%). RPV steels also normally contain significant amounts of trace impurities such as Cu (0.03–0.5%) and P (0.003–0.030%); the higher impurity concentrations are characteristic of welds in older vessels. While vessel heat treatments at around 600°C result in pre-precipitation of

Table 1
Summary of nanofeatures formed in irradiated RPV steels[a]

Description (acronym)	Rad. (nm), Conc. ($/m^3$)	Compositions	Comments
Copper-rich precipitates (CRPs)	0.5–1.5 nm, $0.1–2 \times 10^{24}/m^3$	Cu(> 50%)–Mn/Ni/Si	CRPs rapidly nucleate at Cu > 0.1% growing and finally slowly coarsening near the peak volume fraction
Manganese/nickel-rich precipitates (MNPs)	similar to CRPs	Mn/Ni/Si (> 50%)–Cu	MNPs are favored by high Mn, Ni and low T_i, and Cu and *may* form at low Cu at high ϕt
Vacancy cluster–solute complexes	< 0.5 nm, up to $10^{24}/m^3$	vacancies–Cu/Mn/Ni/Si/...	thermally unstable (dissolve) in typical irradiations, but reach a steady state concentration dependeing on T_i and ϕ; mediate ϕ effects
Nanovoid vacancy complexes	< 1 nm, up to $10^{24}/m^3$	vacancies–Cu/Mn/Ni/Si/...	stable (grow) under irradiation and increase with $\approx \sqrt{\phi t}$ and lower T_i but independent of ϕ
Dilute solute atmospheres	< 2 nm, up to $10^{24}/m^3$	Fe–Cu/Mn/Ni/Si/...	may contain VCCs and NVCs

[a]Other nano-features may include alloy carbonitrides and phosphides as well as interstitial clusters/dislocation loop–solute complexes; however, these features are not normally believed to result in a major contribution to embrittlement in western-type Mn–Ni low alloy steels.

Cu in excess of about 0.3%, the Cu remaining in solution is highly supersaturated, since the equilibrium solubility limit at 290°C is around 0.004% [9–11,13,19]. At Cu contents greater than about 0.1%, radiation enhanced diffusion, arising from excess defects produced by atomic displacements, leads to rapid nucleation and growth of nm-scale coherent (bcc) Cu-rich precipitates (CRPs) [10,13–15,19]. CRPs are alloyed with Mn, Ni and Si and higher alloy Ni leads to higher CRP contents of both Ni and Mn [7,10,13,19]. At certain combinations of high Ni and Mn and/or lower Ti and Cu, the CRPs are replaced by Mn–Ni-rich precipitates (MNPs). Some Cu is believed to be needed to catalyze the nucleation of MNPs. However, even in low Cu steels there is increasing evidence that MNPs may form at high ϕt. Once formed, MNPs would be expected to grow rapidly to large volume fractions, with corresponding high levels of embrittlement [10,13,19]. The sudden appearance of such 'late blooming phases' could constitute a nasty technical surprise.

Hardening observed at low-to-intermediate ϕt in low Cu ($< 0.1\%$) steels is attributed to so called matrix features [1,7,11–17,19]. There are two broad categories of matrix features. Experiments at different ϕ and T_i and low-temperature (290 to 350°C) post irradiation annealing (PIA) studies have clearly shown that thermally unstable matrix features dissolve in situ under 'typical' irradiation conditions, with a characteristic annealing time (τ) of about 3.3×10^5 s at 290°C [6,10,13,20,21]. The unstable matrix features are believed to be small vacancy cluster–solute complexes formed directly in displacement cascades [6,10,13,19,21]. The vacancy cluster complex concentrations increase up to a steady-state value, $N_{vcc} = N_a \sigma_{VCC} \phi \tau$, where σ_{vcc} is the cluster formation cross-section and N_a is the number of atoms per m^3. The vacancy cluster complex are insignificant below about 10^{16} n/m^2 s at 290°C, but are very important at ϕ levels greater than 5×10^{16} n/m^2 s found in some accelerated test reactor irradiations. Of course, N_{vcc} increases with decreasing T_i due to a corresponding increase in τ [8,13,15–17,19–21].

The second category of matrix features includes those that are thermally stable under irradiation. The embrittlement from the stable matrix features decreases with increasing T_i. However, a number of studies have shown that the hardening contribution from the stable features is remarkably independent of ϕ, increasing roughly in proportion to $\sqrt{\phi t}$ [2,7,10,13,15–17,19]. These features are believed to include stable or slowly growing nanovoid-solute complexes nucleated on smaller, subcritical vacancy cluster complexes [10,13,19]. However, there is a growing body of evidence that stable matrix features include rather dilute solute atmospheres, formed by the segregation of Ni and Mn and other solutes in cascades [10,19,22,23]. Dilute solute atmospheres may contain vacancy cluster complexes and/or nanovoid complexes at their cores. Indeed, while these descriptions involve several distinct categories (vacancy cluster complexes, nanovoid complexes and dilute solute atmospheres), in reality there is probably a continuum of matrix features stemming from a common source, namely, displacement cascades.

The matrix features may also include interstitial cluster–solute complexes [10,13,16,19,24–26]. However, while small dislocation loops are observed at relatively high ϕt, they do not appear to play a large role in hardening at typical RPV irradiation conditions. The high probability of thermally stable interstitial cluster formation in cascades would be expected to lead to growth of larger loops. Thus the absence of observable loops may support recent molecular-dynamics observations that interstitials cluster in $\langle 111 \rangle$ crowdion configurations that are highly mobile, undergoing rapid one-dimensional diffusion to sinks [25,26]. The existence and mobility of interstitial clusters is yet to be directly confirmed; and many details, such as interstitial cluster trapping by solutes or solute atmospheres, and the mechanisms of cluster annihilation at sinks, remain to be studied.

3. Continuum modeling of nanostructural evolution

Odette and co-workers have developed detailed models for both Cu and vacancy clustering based on integrating discrete sets of master equations that describe nucleation, growth and coarsening of both the precipitates and nanovoid complexes [10,13,19]. The models show that the nanovoid complexes only nucleate on smaller vacancy cluster complexes produced directly in cascades. The nanovoid complex clustering model rationalizes, at least partially, the T_i dependence of stable matrix features, but does not explain fully the observed low ϕ sensitivity.

Fig. 1a illustrates the nucleation, growth and coarsening clustering model applied to an Fe–0.4% Cu alloy at 290°C. The only critical model parameters are the precipitate–matrix interface energy ($= 0.4$ J/m^2) and the solubility limit for bcc Cu (≈ 60 appm) which are self-consistently computed from thermodynamic data in the literature [10,13]. The ϕt scale is set by using a radiation enhanced diffusion factor, K (see below), of 10^{-38} m^4. The precipitate concentration (N_{crp}) increases rapidly below 10^{22} n/m^2, peaking at about 2×10^{22}/m^3. The volume fraction, f_{crp}, at full precipitation is approached at about 5×10^{22} n/m^2. The average precipitate radius increases with ϕt in stages, reflecting overlapping regimes of nucleation and growth followed by growth and coarsening. Fig. 1b shows the model predictions of N_{crp}, normalized at 10^{23} n/m^2; these predictions are in good agreement with corresponding normalized small angle neutron scattering (SANS) data on CRPs for a variety of pressure vessel alloys with more than 0.24% Cu irradiated at around 290°C. In general, other comparisons of the nucleation, growth and coarsening model predictions of the Cu (and Ni, P and Mn) and T_i dependence of the evolution of precipitates are also in

good semi-quantitative agreement with experimental observations [10,19].

The evolution of the precipitate composition is modeled by tracking the flow of alloy constituent (i) atoms based on their relative chemical potentials ($\mu_{ip/m}$) in matrix (m) solution and in the precipitates (p) [10,13,19,27,28]. The $\mu_{im/p}$ are computed by extended regular solution theory, using excess enthalpies and entropies for binary alloys found in the literature and include the effect of the precipitate–matrix interface energy. Starting off in supersaturated solution, the high $\mu_{Cu,m}$ decreases as Cu flows into the precipitates. The $\mu_{Mn,m}$ is also initially higher than $\mu_{Mn,p}$. However, there is only limited Mn enrichment in the CRPs without Ni and Ni alone does not enrich to any appreciable extent. However, the combination of Ni and Mn is synergistic, due to the strong attractive interaction enthalpy between these elements. High Mn results in Ni enrichment in the CRPs and the higher Ni attracts more Mn. The models show that formation of MNPs, rather than CRPs, is promoted by low T_i and Cu as well as high Ni and Mn. Indeed for some conditions, low concentrations of Cu can lead to very high volume fractions of MNPs. A key unresolved issue is the amount of Cu, if any, needed to nucleate MNPs and the corresponding nucleation ϕt [10,13,19]. Fig. 1c shows that the thermodynamic model predictions (circles) of precipitate compositions are in good agreement with experimental estimates (diamonds) for irradiated alloys with a range of Cu and Ni content.

Application of these kinetic-thermodynamic models to the evolution of precipitates subject to high temperature PIA is also consistent with experiment [10,12,19,21]. This is illustrated in Fig. 1d for a 0.3% (initially in solution) Cu, 0.8% Ni alloy irradiated at 316°C to 8×10^{22} n/m^2 and annealed at 450°C. The model predictions (lines) of coarsening (increase in size and decrease in number density) and partial dissolution of the CRPs are in good agreement with SANS data (symbols). Predictions of composition are also in good agreement with the SANS magnetic-to-nuclear scattering ratio data, which shows that precipitate dissolution is primarily due to a reduction in the precipitates Mn and Ni content.

The precipitate and matrix feature evolution kinetics are coupled if vacancy cluster complexes are present [6,10,13,19]. The distance along a thermodynamically specified path (e.g. for a given composition and T_i) of precipitate evolution (e.g. f_{crp}) is controlled by the product of the radiation enhanced diffusion coefficient (D^*) and irradiation time, D^*t. Taking $D^* \approx K\phi$ the ϕt corresponding to a specified point on the path is determined solely by the radiation enhanced diffusion factor, K. Assuming that K is controlled by the excess vacancy concen-

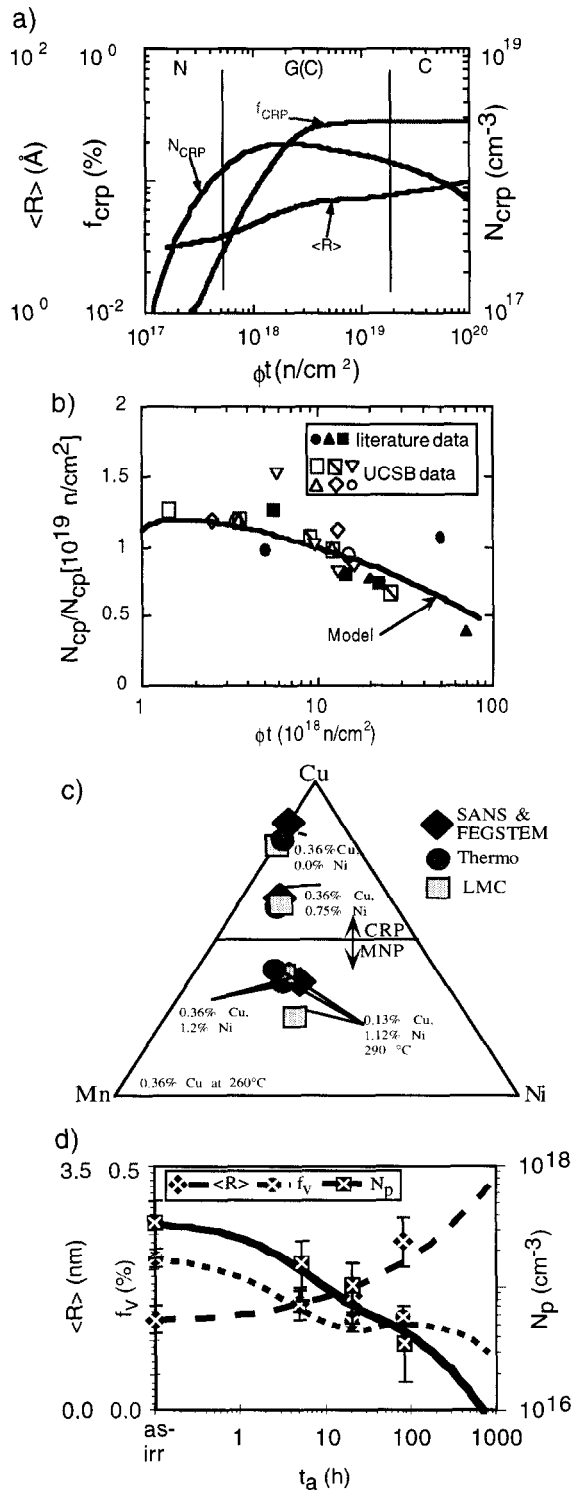

Fig. 1. (a) Clustering model predictions of the evolution of precipitate parameters versus ϕt. (b) Comparison of the model prediction of the normalized number density versus ϕt with SANS data. (c) Comparison of predicated versus measured precipitate compositions. (d) Comparison of predicted versus measured precipitate parameter variations with time for PIA at 450°C (see text for details).

tration at the steady-state balance between generation and annihilation at sinks, which include pre-existing dislocations and vacancy cluster complexes, yields

$$K \approx \eta\sigma_{dpa}/(S_d + \phi 4\pi r_{vcc} N_a \sigma_{vcc}\tau), \quad (1a)$$

where σ_{dpa} is the dpa cross-section, η is the surviving vacancies per dpa following short term recombination in the cascade, S_d is the dislocation sink strength and r_{vcc} is the vacancy cluster complex radius. For very low dose rates $S_d \gg \phi 4\pi r_{vcc} N_a \sigma_{vcc}\tau$ and

$$K \approx \eta\sigma_{dpa}/S_d. \quad (1b)$$

In this case K is independent of ϕ and the precipitate contribution to embrittlement ($D^* t = K\phi t$) depends only on ϕt. For nominal values of $\sigma_{dpa} \approx 1.5 \times 10^{-25}$ m^2, $\eta \approx 0.33$ and $S_d \approx 2 \times 10^{14}$/m^2), $K \approx 2.5 \times 10^{-39}$ m^4. More detailed models (see below) increase the predicted K at low ϕ to about 10^{-38} m^4. At very high dose rates, $\phi 4\pi r_{vcc} N_a \sigma_{vcc}\tau \gg S_d$ and

$$K \approx \eta\sigma_{dpa}/(S_d + \phi 4\pi r_{vcc} N_a \sigma_{vcc}\tau). \quad (1c)$$

In this regime, the precipitate contributions to embrittlement depend only on t rather than ϕt. Thus very high ϕ delays the evolution of CRPs and MNPs to higher ϕt. Assuming $\tau = 3.3 \times 10^5$ s, $r_{vcc} = 5 \times 10^{-10}$ m, $\sigma_{vcc} = 10^{-28}$ m^2, $N_a = 8.5 \times 10^{28}$/m^3, a cluster sink strength equal to S_d occurs at about 10^{16}/m^2 s. The T_i dependence of D^* predicted by a slightly more detailed radiation enhanced diffusion model that also treats Cu-vacancy binding and interstitial diffusion is shown in Fig. 2a for a ϕ of 10^{16} n/m^2 s. Fig. 2b shows the predicted K as a function of ϕ for a range of T_i along with corresponding experimental estimates based on SANS and PIA studies [6,10,13,19,21].

The net effect of ϕ on embrittlement is complex, since the vacancy cluster complexes add directly to hardening but also delay the precipitate contributions [6,9,10,19–21]. Low temperature (290 to 350°C) PIA has been used to discriminate the precipitate, unstable matrix feature and stable matrix feature contributions to hardening [6,9,10,20,21]. An example of the PIA data is shown in Fig. 2c for 343°C PIA hardness recovery of a high 0.35 Cu (bulk), 0.6% Ni weld irradiated at 290°C to about 5×10^{22} n/m^2 at both very high (5×10^{17} n/m^2 – s) and low-intermediate (6×10^{15} n/m^2 s) ϕ. The recovery at 1.8×10^4 s (5 h) is taken as the thermal signal for unstable matrix features; note, similar recovery is observed in about 3.3 ×

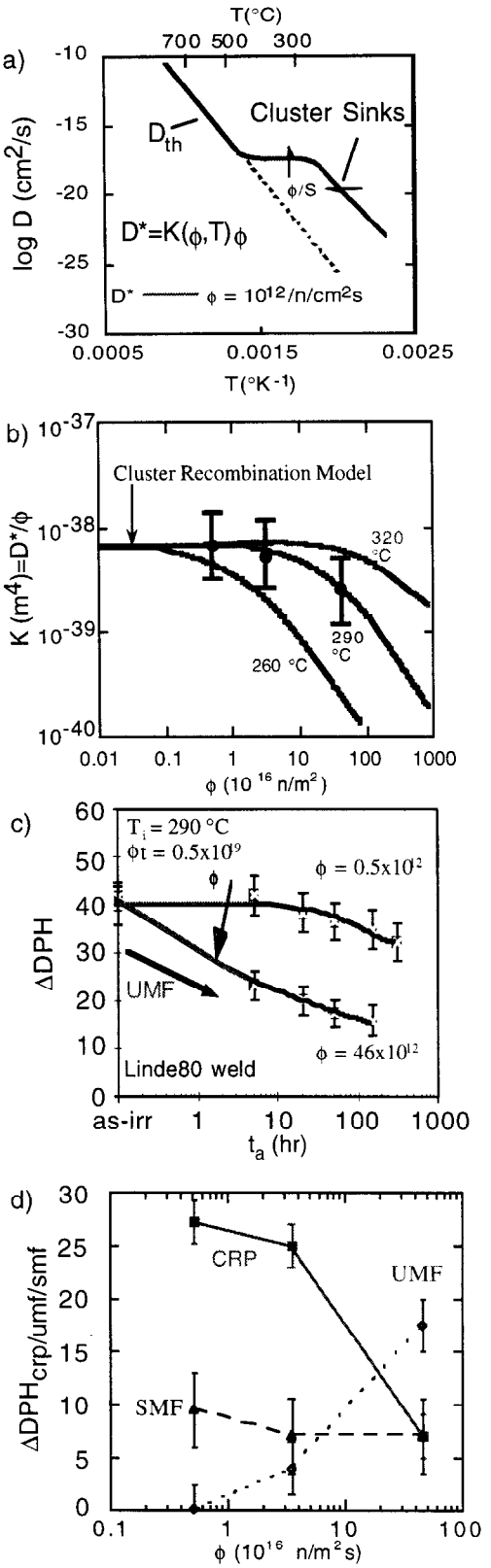

Fig. 2. (a) The predicted temperature dependence of the radiation enhanced diffusion coefficient at 10^{16} n/m^2 s. (b) Comparison of the model prediction of the ϕ and T_i dependence of the radiation enhanced diffusion coefficient factor, K, with estimates from experiment. (c) Hardness recovery for PIA at 343°C showing the effect of ϕ on the unstable matrix feature. (d) The effect of ϕ on the balance of hardening features (see text for details).

10^5 s for PIA at the irradiation temperature of 290°C. Fig. 2c clearly shows that the high ϕ irradiations produce a much larger unstable matrix feature contribution to hardening than are observed in low ϕ irradiations.

A much larger database of these types of measurements was used to estimate the effect of Cu, Ni, T_i, ϕt, as well as ϕ on the balance of various features based on their defined thermal annealing signatures [6,9,10,12,19–21]. These studies showed that: (a) Cu enhances the precipitates (CRPs) and, to some extent, the stable matrix features; (b) Ni enhances precipitates (CRPs and MNPs) and, to some extent, the vacancy cluster complexes; and (c) lower T_i enhance vacancy cluster complexes, and, to some extent, the precipitates. While the stable matrix features continue to increase with ϕt, the hardening contributions from vacancy cluster complexes and precipitates saturate. Most notably, this database has been used to develop a remarkably self-consistent model of ϕ-effects [6,9,14,20,21]. The effect of ϕ is illustrated in Fig. 2d for 290°C irradiations to about 5×10^{22} n/m^2 of high Cu ($\approx 0.3\%$ in solution), intermediate Ni ($\approx 0.6\%$) alloys. Increasing ϕ enhances the unstable matrix features. Since unstable matrix features are vacancy sinks that reduce K (see Eqs. (1a), (1b) and (1c)), higher ϕ reduces (delays) precipitate contributions to hardening. Fig. 2d shows that ϕ has little effect on the stable matrix features. The kinetics of the increase in hardening during irradiation and recovery during PIA ($\tau \approx 3.3 \times 10^5$ s) are consistent with models that assume that the stable matrix features are vacancy cluster complexes [13,20,21]. As illustrated in both Fig. 2b and d, perhaps the most important result is that vacancy cluster complex mediated ϕ effects disappear below about 10^{16} n/m^2 s at 290°C.

Recently a variety of evidence has been reported, including intermediate-term (up to 8000 h) thermal hardening data in high Ni and Cu alloys aged at temperatures between 290 and 350°C, suggesting that there may be a second ϕ-dependent regime at less than about 10^{14} n/m^2 s [11,16,29]. This effect is attributed to anomalous fast solute clustering below about 450°C compared to rates extrapolated from higher temperature data (i.e. the dashed line in Fig. 2a). The high Cu and Ni sensitivity of this effect suggests that there are strong interactions between vacancies and some solutes (e.g. Cu, Mn and Ni) and that highly correlated (versus random) diffusion processes operate at low temperatures.

In summary, thermodynamic and kinetic rate theory models have provided significant insight about embrittlement nanostructures. However, there are a number of important unresolved questions.

(1) A better understanding of the detailed structure and properties of the precipitates is needed to: (a) resolve controversies about the interpretation of SANS and field emission scanning transmission electron microscopy (FEGSTEM) versus atom-probe field-ion-microscopy (APFIM) measurements ([22,27,28] and see below); (b) refine models of precipitate composition and hardening efficiency; and (c) address issues such as the potential for cascade assisted nucleation of MNPs at low Cu levels [19].

(2) It is difficult to have much confidence in the models of matrix features (e.g. unstable matrix features = vacancy cluster complexes?) or the parameters used in these models (e.g., σ_{vcc}), since their identities are yet to be confirmed. Further, while cascades are believed to play a critical role in the formation of matrix features, defect and solute rearrangements during aging (periods up to several hundred thousand seconds) following initial cooling (periods of picoseconds) have not been modeled. Indeed, the conclusion that cascades are needed to form the matrix features is challenged by results of low (≈ 60°C) T_i electron and thermal neutron irradiations, that do not produce cascades, showing hardening comparable to that produced by fast neutrons at the same dpa [30,31].

(3) The fate and character of cascade interstitial clusters and the potential for hardening by these clusters and cluster nucleated dislocation loops is an open question. More detailed discussions of self-interstitial clusters are presented elsewhere [25,26].

4) The hypothesis that complex highly correlated 'fast' diffusion processes may take place in semi-concentrated alloys below about 450°C leading to a low ϕ-dependent regime cannot be modeled using standard rate theory [29].

Further progress in understanding and modeling nanostructural evolution will require additional well-designed experiments coupled with the development and application of advanced methods of atomic scale simulation. The use of atomistic models to provide a theoretically robust and self-consistent interpretation of characterization studies at the nanoscale, has been termed a computational microscope.

4. Atomistic models: Towards a computational microscope

The primary methods of atomic-scale modeling include molecular dynamics and molecular statics as well as various forms of Monte Carlo simulations. It should be emphasized at the outset, that the validity of all of these techniques depends strongly on the accuracy of the underlying descriptions of many-body interatomic interactions. Since rigorous many-body potentials are generally not available, particularly for multicomponent alloys of transition metals such as Fe, our results must be viewed as preliminary and

Fig. 3. (a–d) Typical CRP/MNP structures obtained from LMC simulations for irradiated alloys with a range of Cu and Ni contents (see text for details). (e) LMC prediction of the CRP structure for the B&W surveillance Linde 80 weld.

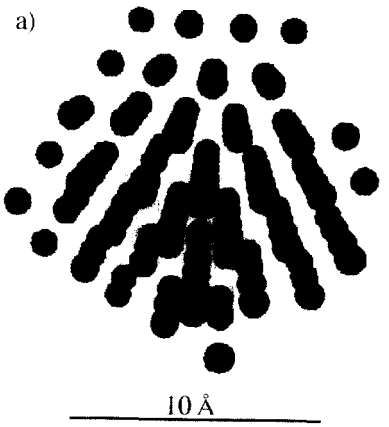

0.4% Cu, 1.4% Mn, 0% Ni, 260 °C

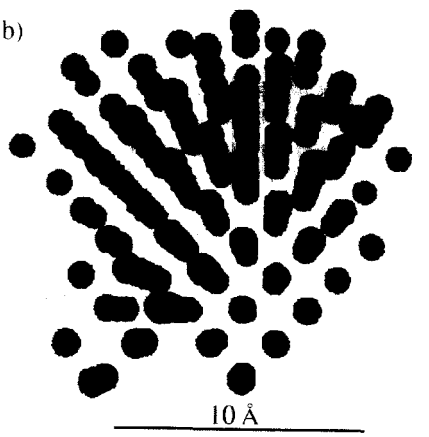

0.4% Cu, 1.4% Mn, 0.75% Ni, 260 °C

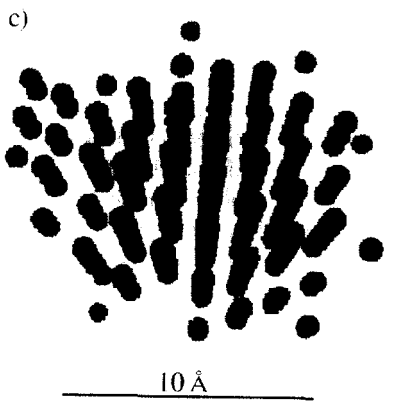

0.4% Cu, 1.4% Mn, 1.2% Ni, 260 °C

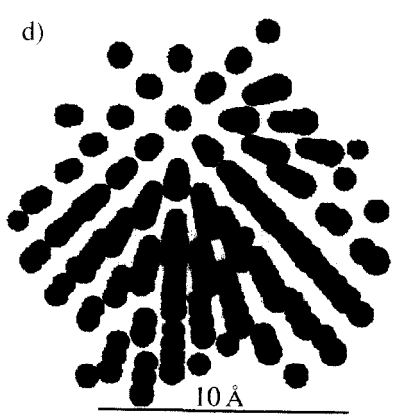

0.15% Cu, 1.4% Mn, 1.12% Ni, 290 °C

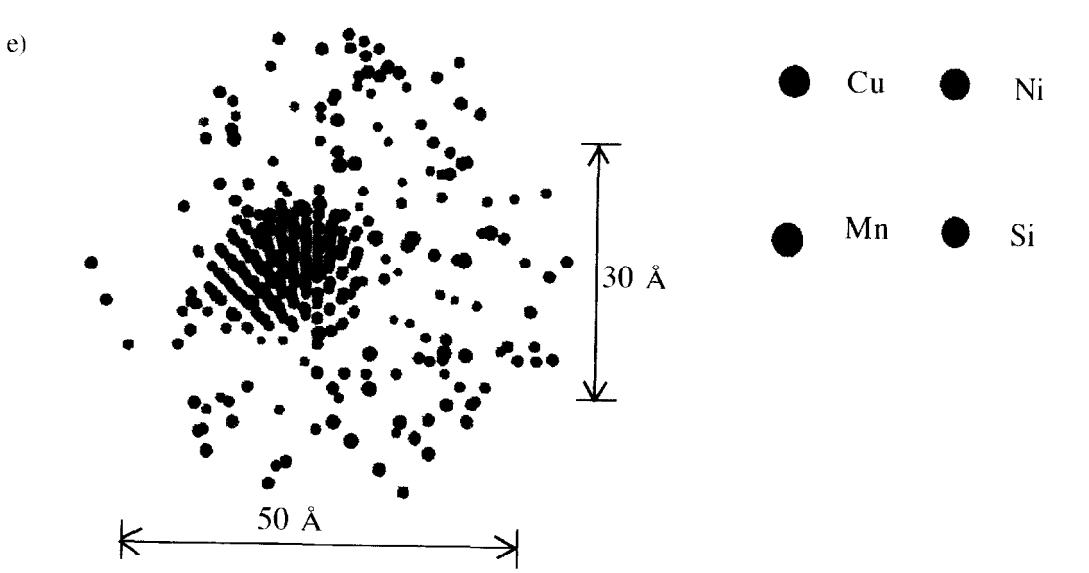

tentative. Nevertheless, using a computational microscope to effectively couple the atomistic simulations to many other sources of information, including experiment, can provide enormous insight about nanostructural evolution processes that cannot be obtained by any other means.

4.1. The composition and structure of nanoprecipitates

Consistent with both coupled SANS/FEGSTEM measurements and mechanical property trends, physical models predict that well formed CRPs are the dominant nanofeature in steels containing more than about 0.1% Cu [9–17,19–21]. However, this view of embrittlement nanostructures has been challenged by Pareige and Miller based on their interpretations of APFIM data [22]. These workers propose that the dominant embrittling features are the dilute solute atmospheres rather than well defined CRPs, even in high Cu steels. Detailed evidence showing the inconsistencies in their interpretation are presented elsewhere [27,28]. However, we review one compelling argument in favor of well formed CRPs based on the unification between theory with both SANS and APFIM measurements provided by the lattice Monte Carlo (LMC) simulation of a 0.24% Cu, 0.56% Ni Linde 80 surveillance weld irradiated at 283°C and 7.4×10^{14} n/m^2 s to 3.5×10^{23} n/m^2.

The LMC model was developed to simulate the detailed atomic scale configuration of the Cu–Mn–Ni–Si features. Due to space limitations, the model is very briefly described here and additional details are presented elsewhere [27,28]. The LMC algorithm is based on exchanging the lattice positions of each solute atom and its neighbors according to a probability (P) defined as the Boltzmann factor, $P = \exp(-\Delta G'/kT)$ for $\Delta G' > 0$ or 1 for $\Delta G' \leq 0$; this is the well known Metropolis criteria. Ideally G' represents all sources of enthalpy/thermal entropy and $\Delta G'$ is the change in this total energy associated with a particular atomic exchange. The system evolves towards the lowest free energy (G) state, $G = G' - TS_{con}$, where the configurational entropy (S_{con}) is simulated by the Boltzmann weighting algorithm. Typical simulations start out as random solid solutions that evolve through stages of quasi-nucleation, growth and coarsening, ultimately forming a single fluctuating feature.

In this work, the G' were approximated using pair bond (G_{ii}, G_{ij}) potentials. These potentials, derived from empirical thermodynamic data (excess enthalpies and entropies) based on the regular solution theory approximations, are given in Ref. [28]. The only significant adjustment of the empirical data involved the Mn–Ni interaction. The nominal values in the literature produced much higher Mn and Ni contents in the precipitates than those that have been experimentally observed. An adjustment factor of 0.7 provides good agreement between the thermodynamic predictions (circles) and SANS data (diamonds) of irradiated alloys with a range of Ni and Cu contents shown in Fig. 1c. Thus this same adjustment was also used in the LMC simulations.

As also demonstrated in Fig. 1c, the LMC predictions of the precipitate compositions (squares) are in reasonable agreement with both the thermodynamic calculations (circles) and experimental estimates (diamonds). However, the LMC simulations show that the precipitates manifest a variety of complex chemical structures depending on the Cu, Ni, Mn contents and temperature. In general, the solute clusters are fairly compact, with well defined, nearly pure Cu cores, surrounded by shells and/or appendages that are rich in Mn and Ni. The Mn–Ni appendages are ordered. Typical CRP morphologies resemble irregular polyhedra with faceted {110} faces truncated by {100} caps. Representative precipitate configurations from the LMC simulations of the same irradiated alloys as cited in the previous section are shown in Fig. 3, and can be summarized as follows. In the case of the 0.4% Cu 1.4% Mn (bulk) steels irradiated at 260°C containing various amounts of Ni: (a) the CRP for 0% Ni (Fig. 3a) has a Cu core surrounded by a patchy shell of Mn; (b) the CRP for 0.75% Ni (Fig. 3b) has a Cu core surrounded by a patchy shell richer in both Mn and Ni; (c) the MNP/CRP for 1.2% Ni has an ordered Mn–Ni appendage epitaxial to a nearly pure Cu region, again surrounded by a patchy Mn and Ni shell. The MNP structure for the 0.15% Cu, 1.12% Ni steel irradiated at 290°C (Fig. 3d) consists of a very small Cu core surrounded by an ordered Mn–Ni region containing a few dissolved Cu atoms.

With this basic 'calibration' the LMC model was used to simulate the precipitate structures in the irradiated Linde 80 surveillance weld described above. This weld has been characterized by both APFIM [22] and SANS [27,28]. The APFIM study by Pareige and Miller is particularly notable, since it included, by good fortune, a feature within a nominal 2.5 nm aperture oriented such that it allowed a complete (020) plane-by-plane analysis. In principle, this permits atomic level resolution of the features' composition along the ⟨010⟩ axis. The FIM mode revealed an approximately 2.9 nm darkly imaging feature. Pareige and Miller interpreted their results as demonstrating that this feature is a dilute solute atmosphere. Based on a cylindrical volume of about 2.9 nm high and 2.5 nm in diameter, the average Fe content is about 77%. The corresponding concentrations of the solutes (and enrichment factors in parenthesis) are: 8.5% Cu (116); 5.6% Mn (5); 4.4% Ni (9); 4.1% Si (2).

The Pareige and Miller analysis is based on the assumption that the solutes are distributed randomly in the area of the (020) planes sampled by the APFIM aperture. However, a random distribution is actually inconsistent with their own layer-by-layer analysis, which shows a Cu rich core. Indeed, assuming a polyhedral Cu core and a Mn–Ni–Si rich outer shell yields reasonably good agreement with the sequence of atom counts in the APFIM study.

A SANS study on the same material yielded cross-sections consistent with a log normal distribution of $3.5 \times 10^{23}/m^3$ well formed CRPs with a volume fraction of 0.38% and a volume weighted average radius of 1.38 nm. The magnetic to nuclear ratio (M/N) measured in SANS studies can be used to estimate the composition of the scattering features. Assuming the precipitate is composed of Cu, Mn, Ni (= Mn/2), the measured value of M/N ratio of about 2.08 is consistent with a CRP composition of about 70% Cu. Assuming a Cu, Mn, Ni (= Mn/2), Si (= Ni) precipitate, the experimental M/N is consistent with 65% Cu. Note that the SANS data probably contains a small contribution (< 0.05% volume fraction) from the matrix features, which may include dilute solute atmospheres.

The APFIM versus SANS/thermodynamic views of the nanofeature are reconciled by the direct LMC simulations. In this case Si has been added to the simulation [27,28]. Fig. 3e shows a snapshot of a typical CRP, showing a Cu rich core surrounded by a Mn–Ni–Si rich shell. A sphere of diameter 1.6 nm centered on the polyhedral CRP encloses an average composition of 59% Cu, 5% Ni, 5% Si, 23% Mn and 8% Fe. The (020) layer-by-layer cumulative atom count from the LMC simulation is in good agreement with the APFIM [27,28]. The simulated SANS cross-sections for this structure, calculated using the Debye equation to model scattering from the specific arrangement of atoms predicted by the LMC simulation, are also in excellent agreement with the SANS measurements [27,28].

The LMC method presented here is basically an algorithm that uses empirical thermodynamic data to model evolution to local configurational equilibrium in nanoprecipitates at or near atomic scale resolution. Of course, the accuracy of the results is limited by the accuracy of the interatomic potential model. However, the consistency between LMC, APFIM and SANS represents an important unification of experiment with basic physical principles.

4.2. Vacancy cluster complexes and cascade aging

Issues associated with matrix features, cascade enhanced nucleation of MNPs and complex low temperature diffusion processes require the development of new atomic-scale models. A key issue is determining the role of the processes that occur during the formation, cooling and, particularly in the subsequent aging stage, of displacement cascades in multicomponent alloys. Molecular dynamics (MD) simulations of cascades in pure iron are consistent with the classical picture of a vacancy rich core surrounded by an interstitial rich shell [24]. A large fraction of the interstitials are clustered in ⟨111⟩ crowdion orientations [24–26]. These clusters, in the form of small highly kinked dislocation loops, are highly mobile and diffuse in ⟨111⟩ directions [25,26]. Small 2–3 member interstitial clusters can reorient to new ⟨111⟩ directions in MD picosecond time-scales; however, larger interstitial clusters are limited to one-dimensional motion along a single glide prism [26].

There are a number of significant conceptual consequences of the diffusion characteristics of the interstitial-clusters. First, the directionality of diffusion may limit vacancy-interstitial recombination during cascade cooling and aging; second, their high mobility separates the time scales over which the fate (recombination or diffusion away from the cascade) of interstitial features is determined relative to vacancies. Thus, at least to first order, cascade vacancy and interstitial aging processes can be modeled separately. The first stage involves full MD simulations of the short-term, post cooling stage, where cascade recombination and interstitial diffusion away from the cascade occurs with the vacancies frozen in place; the second stage involves the rearrangement and clustering of vacancies without any interstitials present.

Most MD simulations of cascades in Fe have not shown much nascent cascade vacancy clustering [24]. However, many of the cascade vacancies are within only one or two jump distances from each other [25]. Hence, clustering is likely to occur during the subsequent cascade aging stage. Conceptually, the sequence-of-events during aging involves the formation of small vacancy clusters, which dissolve rapidly and/or coarsen partially, but eventually dissolve fully leading to vacancy annihilation at fixed sinks. In pure Fe, this process is expected to be fairly rapid around 290°C, taking place in several thousand seconds or less.

However, in alloys cascade vacancy clustering inherently involves the co-diffusion of solute atoms. The potential for vacancy cluster complex formation in Fe–Cu alloys has been previously modeled using coupled diffusion equations that track the flows of both vacancies and solute–vacancy complexes [32]. This model predicted the formation of small vacancy clusters partially coated by Cu, e.g. vacancy cluster complexes. The corresponding reduction in the surface energy results in large increases in the vacancy cluster-complex lifetime. Elements such as Mn, Ni, Si and P would be expected to play a role that is qualitatively similar to Cu. Metastable vacancy cluster-complex lifetimes would be further extended by additional segregation of interstitial elements such as C and N, enabled by the initial cascade segregation of substitutional solutes.

A much better approach to modeling the co-clustering is provided by LMC simulations which can track directly the coupled motion of vacancies and solute atoms. However, reliable simulations of solute diffusion and clustering require accurate multi-element many-body interatomic potentials. For example, solute diffusion in bcc structures inherently involves jumps to second nearest neighbor sites and diffusion models require knowledge of at least five independent jump frequencies [33]. Clearly, simple pair potentials do not provide the necessary information. In this work, many-body potentials based on the embedded atom

Table 2
Lattice EAM potentials

Inter-action	V_1 (eV)	V_2 (eV)	V_3 (eV)	ϕ_i^2 (eV^2)	ϕ_3 (eV^2)	ϕ_3 (eV^2)
Fe–Fe	0.0907	−0.0311	–	1.786	1.068	–
Cu–Cu	0.2520	0.0340	0.0269	2.043	0.938	0.0108
Fe–Cu	0.2350	0.0290	–	1.910	1.001	–

method (EAM) were used to describe the Fe–Fe, Cu–Cu and Cu–Cu interactions. These interactions depend on the local environment out to second (third for Cu–Cu) nearest neighbor.

The lattice EAM potentials were computed at the first, second (and third for Cu–Cu) nearest-neighbor distances in the bcc iron lattice. The total energy of an atom (E_i) is given by

$$E_i = 0.5\left[\sum_{1-8}(V_{i1}) + \sum_{1-6}(V_{i2}) + \sum_{1-12}(V_{i3})\right] - \left[\sum_{1-8}(\phi_{i1}) + \sum_{1-6}(\phi_{i2}) + \sum_{1-12}(\phi_{i3})\right]^{1/2}, \quad (2)$$

where the V are the pair potentials and the ϕ the electronic embedding terms. The Vs and ϕs for bcc Fe and Cu were based on the EAM potentials of Finnis and Sinclair as modified by Calder–Bacon (Fe–Fe) and Ackland et al. (Cu–Cu) [34–36]. We developed the Fe–Cu interaction potential by fits to the heat-of-solution for Cu in Fe, the Cu-vacancy binding energy and the (110) Fe–Cu interface energy [37]. The many-body electronic contribution of the Fe–Cu potential was fixed at the geometric mean of the corresponding potentials for Fe and Cu, $\phi_{Fe-Cu} = (\phi_{Fe-Fe}\phi_{Cu-Cu})^{1/2}$ [38]. The lattice potential is summarized in Table 2. This potential gives the following unrelaxed material properties: Fe and Cu bcc cohesive energies, 4.28 and 3.43 eV/atom; Fe vacancy formation energy, 2.05 eV; dilute heat of solution of Cu in Fe, 0.536 eV/atom; Cu-vacancy binding energy at first and second nearest neighbor, 0.12 and 0.08 eV; Fe–Cu (110) interface energy, 0.3 J/m^2; Cu–Cu binding energy at first and second nearest neighbor, 0.129 and 0.056 eV. The potential should definitely be considered as approximate. Indeed, the major implications of the results should be viewed as identifying potentially significant phenomena, rather than quantitative simulations of actual physical processes.

The LMC cascade aging simulations were carried out as follows. The eight Boltzmann jump probabilities for each cascade vacancy were computed and summed to find the total probability of a specified vacancy jump assuming a constant 0.9 eV activation barrier. The probabilities (much less than 1) were normalized to the highest total jump probability. The absolute probability of this vacancy exchange then sets the effective 'time-step' for a sweep of all the other vacancies with a lower probability of jumping. The specific jump for the vacancy with a normalized probability of 1 was selected based on a standard random number test. A random number Metropolis criteria test was then applied to see if the other vacancies jumped and, if so, which particular exchange they selected. In principle, the effect of the first and subsequent jumps on those that may succeed them should be evaluated. While not done in the current version of the simulation, this approximation should have little effect on the overall results. Thus at least one, and in some cases more than one, vacancy jump occurs in each LMC sweep. For example, in the case of isolated vacancies in pure iron, all of them jump in each sweep. Of course, a more rigorous residence time algorithm could be applied to provide a slightly more realistic simulation; however, our simpler approach is believed to be a good approximation to the actual sequence-of-events during cascade aging.

Since the total probability of vacancy jumps depends on the local environment, including the effects of other vacancies and solutes, the time increment changes between sweeps. The increments generally start out short, when the vacancies are isolated and not bound to each other or Cu, but increase enormously as growing cluster-complexes evolve (note, when a vacancy is emitted from a cluster-complex and migrates through the lattice, the sweeps revert to a much shorter time step). The simulation cell boundary is assumed to be a sink, so the vacancies that do not cluster are ultimately annihilated. Thus after the initial clustering, coarsening competes with vacancy emission-annihilation. As the cluster-complexes grow to larger sizes, non-emission jumps that change the shape, but not the cluster-complex size, become far more probable than emission. The shape changes lead to significant cluster-complex mobility at smaller sizes; and the initial coarsening occurs by cluster-complex coalescence as well as single vacancy emission–absorption events.

When there are only a few larger coarsened cluster-complexes left, the probability of shape changes is much higher than for emission, but the cluster mobility drops. In this stage the efficiency of the isothermal LMC algorithm decreases dramatically. Thus to get to the point of complete dissolution, the vacancy with the highest probability

Fig. 4. A typical LMC simulation of aging of a 20 keV cascade supplied by Stoller in a 0.4% Cu alloy producing various vacancy cluster–solute complexes: (a) the original cascade; (b) an intermediate stage with six cluster-complexes; (c) an intermediate stage with four cluster-complexes; (d) a Cu–vacancy cluster-complex at the four cluster stage; (e) the final two cluster-complexes; (f) the Cu clusters formed (isolated, other Cu atoms are not shown) after final dissolution of the last 19 vacancy cluster-complexes.

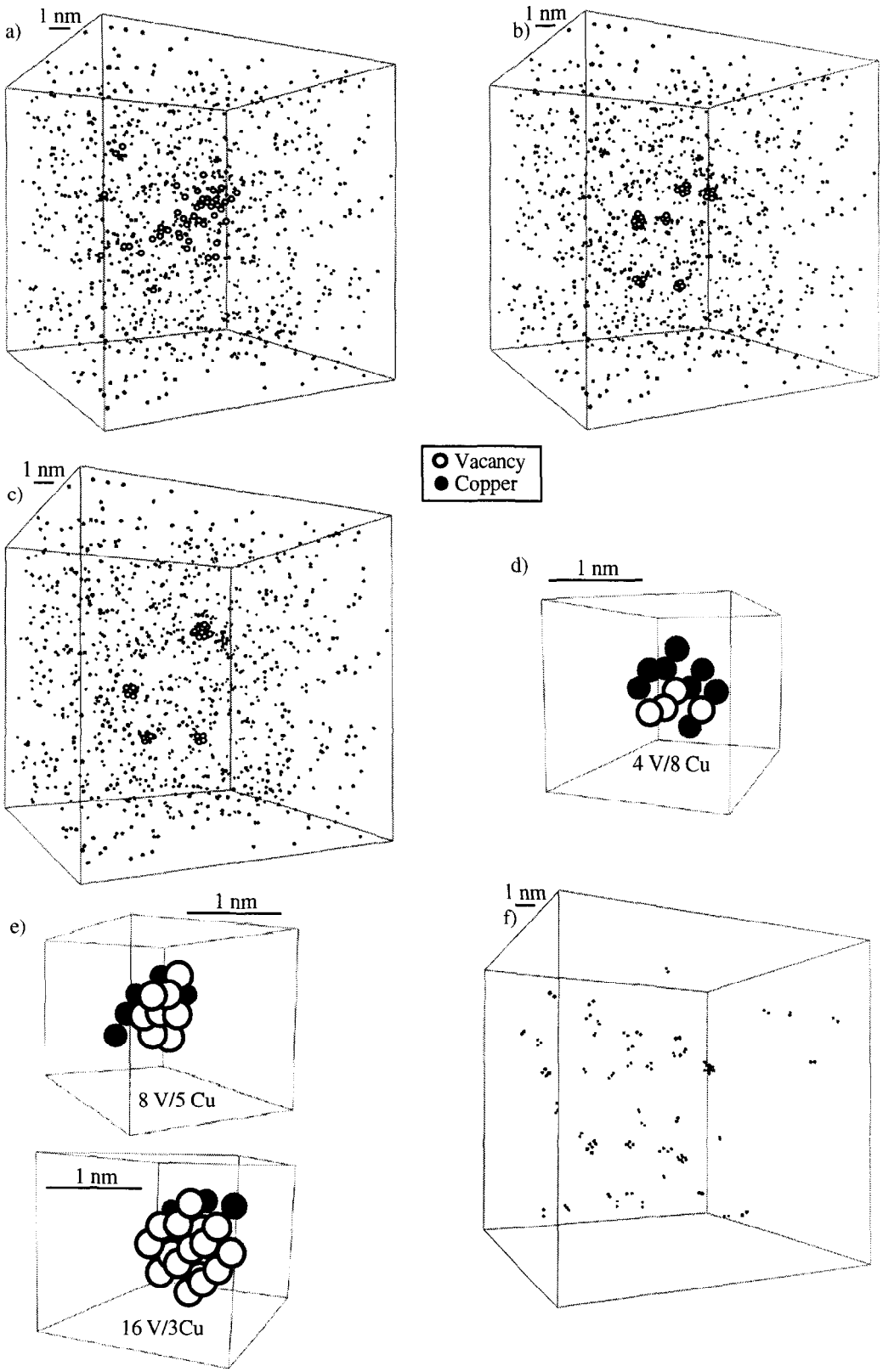
a)
1 nm
b)
1 nm
Vacancy
Copper
c)
1 nm
d)
1 nm
4 V/8 Cu
e)
1 nm
8 V/5 Cu
1 nm
16 V/3Cu
f)
1 nm

of taking the first jump away from the cluster-complex to a higher energy position was identified. An additional four jumps along the highest probability path away from the cluster was then imposed to increase the likelihood of vacancy escape. The LMC simulation was then run until the fate of the free vacancy was determined. If this vacancy rejoined its original cluster-complex the LMC increment was repeated. Otherwise the vacancy joined another cluster-complex or was annihilated. An estimate of the corresponding time increment could be based on the probabilities of the sequence-of-jumps. However, since this does not include all the combinatorial possibilities, we focus here only on the clustering outcome, rather than the absolute time scale for large cluster-complex dissolution. This procedure was repeated until complete vacancy dissolution. Note, an automated approach under development, based on pulse annealing of the clusters, is expected to yield somewhat more quantitatively reliable, but qualitatively similar, results.

The following discussion primarily involves simulations of a 20 keV MD cascade run out to 200 ps provided by Stoller. Given the quasi one-dimensional diffusion of the interstitial clusters and the excess of single interstitials associated with the periodic MD boundary conditions, further recombination is believe to be minimal and was neglected. The LMC simulations started with 47 vacancies, an upper bound which is believed to be close to the actual value. In the future, other Monte Carlo simulations or longer MD runs will be carried out to more rigorously account for this transition phase of cascade evolution. The cascade studies were supplemented by a variety of 'longer-term' studies of clustering phenomena produced by different numbers of vacancies (1–3) in simulation cells with various sizes, Cu contents and over a range of temperatures. The most significant qualitative observations can be summarized as follows.

(1) One or more Cu atom may be bound in mobile complexes containing up to about five vacancies. Cluster-complexes with larger numbers of vacancies are much less mobile.

(2) The mobile V–Cu complexes, including those formed in cascades, contribute to the formation of small Cu clusters. The process can be viewed as vacancy cluster scavenging of Cu.

(3) Single or few vacancy clusters are also bound to Cu-clusters that may be much larger. The Cu–vacancy (as opposed to a vacancy–Cu) complexes can also diffuse, as an entity, by interface motion and solute exchanges with vacancies on the periphery of the cluster. Thus growth and coarsening may involve solute cluster coalescence, as well as single Cu atom impingement-emission processes. The Cu–vacancy cluster mobility decreases rapidly with the complex size.

(4) The vacancy cluster-complexes grow to a range of relatively large sizes (up to ≈ 20 vacancies) and are associated with a smaller number of co-segregated Cu atoms (depending on the alloy composition).

(5) The clustering and co-segregation does not appear to result in any significant long range Cu transport into the core region of the cascade. However, 1–2 nm regions of significant Cu enrichment, by factors of about 2 to 10, were found in the higher Cu alloy. These may be the precursor to dilute solute atmospheres that evolve further during the subsequent stages of long range radiation enhanced diffusion. Note that atom transport by cascade interstitials may also contribute to solute enrichment.

(6) The simulations revealed highly coordinated vacancy–solute diffusion mechanisms that may also help to rationalize the fast low temperature diffusion/aging effects cited above. A hypothesis is that in semi-concentrated alloys (e.g., Ni + Mn + Cu + Si > 2%) processes like diffusion of solute clusters due to a single or a few attached vacancies and self-organization of solute enriched regions that act as preferred chemical channels for vacancy diffusion can greatly accelerate clustering and precipitation.

The formation of cluster-complexes is illustrated in Fig. 4 for a typical LMC sequence at 290° in a 250 000 atom simulation cell for the 20 keV cascade in an alloy with 0.4% Cu. The nascent cascade with 47 vacancies (Fig. 4a) initially results in the formation of eight complexes, containing an average of 4.9 vacancies and 1.4 Cu atoms. The smallest tri-vacancy clusters quickly dissolve with three vacancies joining the six remaining clusters and three annihilating (Fig. 4b). The smaller complexes are mobile and diffuse as an entity, scavenging Cu along the way. This continues to a point when two cluster-complexes with six and eight vacancies coalesce. The somewhat larger clusters are less mobile and one cluster dissolves. The four remaining clusters contain an average of 7.2 vacancies and 4.8 Cu atoms (Fig. 4c), including a complex with four vacancies and eight Cu atoms (Fig. 4d). The cluster-complexes that emit all their vacancies leave behind bare Cu clusters. The final two cluster-complexes contain eight plus five and 16 plus three vacancy plus Cu atoms, respectively (Fig. 4e). These cluster-complexes were very stable; thus, the eight vacancy cluster was dissolved first by the probability path method, described previously. Before its final vacancy dissolution, the size of the large cluster-complex increased to 19 vacancies, with the other five vacancies undergoing annihilation at the cell boundary.

Clearly the cascades also induced substantial Cu clustering as well as vacancy clustering. A 5 nm sphere

Fig. 5. Snapshots from a LMC simulation of the Cu cluster evolution in an Fe–0.6% Cu alloy containing one vacancy in a cell with 16 000 atoms (see text for details).

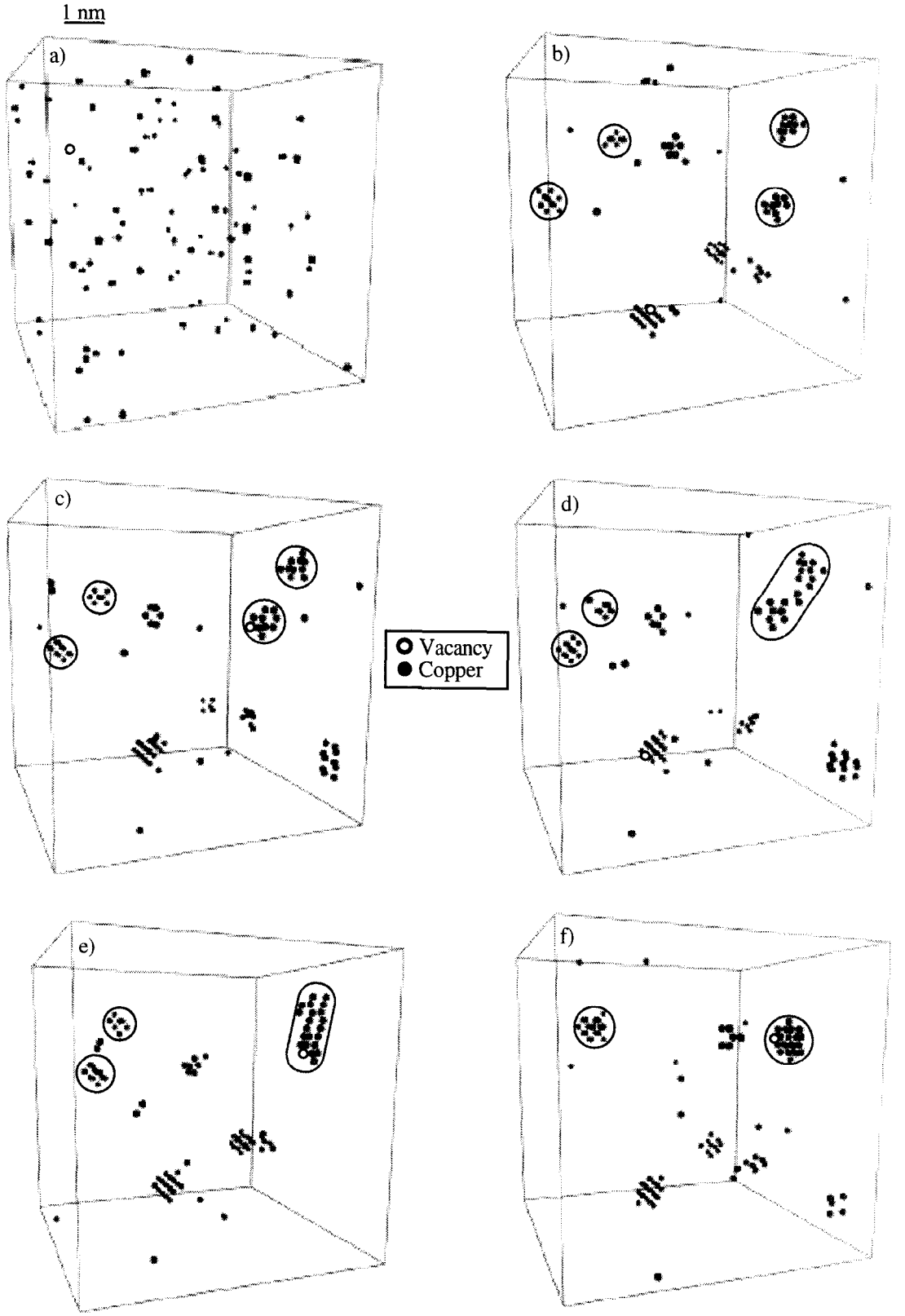
1 nm
a)
b)
c)
d)
Vacancy
Copper
e)
f)

centered around the core of the cascade initially had eight first and 0 second nearest neighbor Cu–Cu bonds. Following cascade aging the number of first and second nearest neighbor bonds increased to 87 and 28, respectively. The corresponding bond numbers for a 2% Cu alloy were initially 155 and 83, increasing to 967 and 490 after aging. Thus, as expected, the clustering increases roughly with the square of alloy Cu content. The final distribution of Cu atoms with Cu nearest neighbors (for clarity, the other Cu atoms are not shown) in the 0.4 alloy is shown in Fig. 4f. Clusters with up to eight Cu atoms, along with numerous smaller Cu aggregates, are formed during cascade aging. Even larger and more numerous Cu clusters form in the 2% solute alloy, where the Cu is expected to act as a crude surrogate for Mn, Ni and Si. These solute clusters would be expected to serve as preferred nucleation sites for both CRPs and MNPs. Cascades and clustering also appear to produce locally enriched regions that resemble dilute solute atmospheres, or their precursors. However, additional statistical and geometric analysis and models which include individual Ni, Mn and Si potentials will be required to confirm this preliminary indication.

Fig. 5 shows the simulation snapshots of the Cu clustering in an Fe–0.6% Cu alloy produced by up to 3×10^7 jumps of a single vacancy in a small cell with 16 000 atoms. Starting from random solid solution (Fig. 5a) the vacancy diffusion produces a number of small Cu-clusters (Fig. 5b). The vacancy is tightly bound to the Cu clusters (Fig. 5c); as a consequence, the Cu-clusters are mobile (Fig. 5b to f). Some clusters eventually coalesce when they approach within a distance with a high probability that the vacancy is shared between them (Fig. 5d to f). The Cu-cluster mobility decreases with increasing size (Fig. 5e to f).

These results should not be taken too literally. They are meant to illustrate potential phenomena, rather than detailed quantitative conclusions. Clearly, however, more realistic models must consider such phenomena, that can only be treated by atomistic-type simulations.

5. Summary and conclusions

The results of this research supports the following tentative conclusions.

(1) In intermediate-to-high Cu steels, CRPs/MNPs are well formed precipitates, albeit with complex chemical structures.

(2) Metastable vacancy cluster–solute complexes are formed in displacement cascades. Continuum clustering models predict that stable nanovoid complexes nucleate on some of the vacancy cluster-complexes.

(3) Cascades also produce a significant amount of Cu (and presumably other solute) clustering. Thus in high Ni steels, cascades may promote the formation of MNPs that could ultimately result in high levels of hardening and embrittlement even at low Cu levels.

(4) The local clustering produced in alloys with Ni, Mn and Si may also be responsible for the formation of dilute solute atmosphere, or their precursors. However, confirmation of this hypothesis will require additional research.

(5) The highly correlated vacancy-solute transport processes illustrated in Fig. 5 may help to rationalize the fast low temperature diffusion and thermal aging phenomena noted above.

It is important to emphasize that this paper describes work that is 'still in progress'. Clearly, much more research will be needed to provide a more complete and reliable quantification. Further development of the computational microscope, marrying atomistic simulations with other sources of information, will help to provide such quantification. While the results outlined here are specific to the problem of irradiation embrittlement of RPV steels, the approaches are pertinent to a wide range of nanostructural processes including those encountered in fusion environments.

Acknowledgements

The authors thank Dr. Roger Stoller (Oak Ridge National Laboratory, ORNL) for providing cascades and, along with Dr. Mike Miller (ORNL), assisting in the acquisition of the layer-by-layer APFIM data. We also acknowledge our former University of California Santa Barbara (UCSB) colleagues, Dr. Chun Li Liu, for his primary role in the development of the LMC simulations and Dr. Bing Ling Chao and Dr. Erik Mader for their major contributions to developing the continuum thermodynamic/kinetic models. We also express our appreciation to UCSB Professors Gene Lucas and Dimititrios Maroudas for many helpful discussions and suggestions. This work was sponsored by the US Nuclear regulatory Commission, Contract No. NRC-04-94-049. The encouragement and support of our program monitors, Mr. Al Taboada and Dr. Mike Vassilaros are greatly appreciated.

References

[1] G.R. Odette, G.E. Lucas, in: J.T.A. Roberts, J.R. Weeks, G.J. Theus (Eds.), Proc. 2nd Int. Symp. on Environmental Degradation of Materials in Nuclear Reactors–Water Reactors (American Nuclear Society, LaGrange Park, IL, 1986) p. 345.

[2] T.J. Williams, P.R. Burch, C.A. English, P.H.N. de la cour Ray, in: G.J. Theus, J.R. Weeks (Eds.), Proc. 3rd Int. Symp. on Environmental Degradation of Materials in Nuclear Reactors–Water Reactors (The Metallurgical Society, Warrendale, PA, 1988) p. 121.

[3] G.R. Odette, G.E. Lucas, Embrittlement of LWR Pressure Vessel Steels, EPRI NP 6114, Electric Power Research Institute, 1989.

[4] G.R. Odette, G.E. Lucas, in: G.J. Theus, J.R. Weeks (Eds.),

Proc. 3rd Int. Symp. on Environmental Degradation of Materials in Nuclear Reactors–Water Reactors (The Metallurgical Society, Warrendale, PA, 1988) p. 345.
[5] G.R. Odette, G.E. Lucas, in: N.H. Packan, R.E. Stoller, A.S. Kumar (Eds.), The Effects of Radiation on Materials: 14th Int. Symp., ASTM-STP-1046 (American Society for Testing and Materials, Philadelphia, PA, 1990) p. 323.
[6] G.R. Odette, E.V. Mader, G.E. Lucas, W.J. Phythian, C.A. English, in: D.S. Gelles, R.K. Nanstad, E.A. Little (Eds.), The Effects of Radiation on Materials: 16th Int. Symp., ASTM-STP-1175 (American Society for Testing and Materials, Philadelphia, PA, 1993) p. 323.
[7] T.J. Williams, W.J. Phythian, in: D.S. Gelles, R.K. Nanstad, A.V. Kumar, E.A. Little (Eds.), Effects of Irradiation on Materials: 17th Int. Symp., ASTM STP 1270 (American Society for Testing and Materials, West Conshohoken, PA, 1996) p. 191.
[8] G.R. Odette, G.E. Lucas, D.K. Klingensmith, in: D.S. Gelles, R.K. Nanstad, A.V. Kumar, E.A. Little (Eds.), Effects of Irradiation on Materials: 17th Int. Symp., ASTM STP 1270 (American Society for Testing and Materials, West Conshohoken, PA, 1996) p. 606.
[9] G.R. Odette, G.E. Lucas, Current understanding of the effects of environmental and metallurgical variables on RPV embrittlement, Proc. of the US NRC 24th Water Reactor Safety Information Meeting, vol. 2, NUREG/CP-0157-2, 1997, p. 1.
[10] G.R. Odette, G.E. Lucas, Recent progress in understanding reactor pressure vessel steel embrittlement, Radiat. Eff., in press.
[11] E.D. Eason, J.E. Wright, G.R. Odette, Improved Embrittlement Correlations for Reactor Pressure Vessel Steels, NUREG/CR-6551, in press.
[12] E.D. Eason, J.E. Wright, G.R. Odette, E. Mader, Models for Embrittlement recovery Due to Annealing of Reactor Pressure Vessel Steels, NUREG/CR-6327, 1995.
[13] G.R. Odette, Modeling irradiation embrittlement in reactor pressure vessel steels, Neutron Irradiation Effects in Reactor Pressure Vessel Steels and Weldments, IAEA Technical Report Series, Vienna, to be published.
[14] G.R. Odette, Scr. Met. 11 (1983) 1183.
[15] G.R. Odette, G.E. Lucas, in: L.E. Steele (Ed.), Radiation Embrittlement of Reactor Pressure Vessel Steels: An International Review, vol. 2, ASTM-STP-909 (American Society for Testing and Materials, Philadelphia, PA, 1986) p. 206.
[16] S.B. Fisher, J. T Buswell, Int. J. Pres. Ves. Piping 27 (1987) 91.
[17] J.T. Buswell, R.B. Jones, in: D.S. Gelles, R.K. Nanstad, E.A. Little (Eds.), The Effects of Radiation on Materials: 16th Int. Symp., ASTM-STP-1175, American Society for Testing and Materials, Philadelphia, PA, 1993) p. 424.
[18] G.R. Odette, P.M. Lombrozo, R.A. Wullaert, in: F.A. Garner, J.A. Perrin (Eds.), The Effects of Radiation on Materials: Effects of Irradiation on Materials: 12th Int. Symp., ASTM-STP-870 (American Society for Testing and Materials, Philadelphia, PA, 1985) p. 841.
[19] G.R. Odette, in: I.M. Robertson, L.E. Rehn, S.J. Zinkle, W.J. Phythian (Eds.), Microstructure of Irradiated Materials, MRS Symposium Proceedings 373 (Materials Research Society, Pittsburgh, 1995) p. 137.
[20] E.V. Mader, PhD dissertation, Department of Materials, University of California, Santa Barbara, 1995.
[21] E.V. Mader, G.R. Odette, G.E. Lucas, in: R.E. Gold, E.P. Simonen (Eds.), Proc. 6th Int. Symp. on Environmental Degradation in Nuclear Power Systems, Water Reactors (The Metallurgical Society, Warrendale, PA, 1993) p. 739.
[22] P. Pareige, M.K. Miller, Appl. Surf. Sci. 94–95 (1966) 370.
[23] S. Miloudi, B. Remmerie, J.C. Van Duysen, in: R.K. Nanstad, M.L. Hamilton, F.A. Garner, A.S. Kumar (Eds.), Effects of Irradiation on Materials: 18th Int. Symp., ASTM STP 1325 (American Society for Testing and Materials, West Conshohoken, PA) accepted.
[24] R.E. Stoller, in: I.M. Robertson, L.E. Rehn, S.J. Zinkle (Eds.), Microstructure of Irradiated Materials, MRS Symposium Proceedings (Materials Research Society, Pittsburgh, 1995) p. 21.
[25] R.E. Stoller, G.R. Odette, B.D. Wirth, Primary damage formation in bcc iron, J. Nucl. Mater., these Proceedings, p. 49.
[26] B.D. Wirth, G.R. Odette, D. Maroudas, G.E. Lucas, J. Nucl. Mater. 244 (1997) 185.
[27] G.R. Odette, C.L. Liu, B.D. Wirth, On the composition and structure of nanoprecipitates in irradiated pressure vessel steels, in: I.M. Robertson, G.S. Was, L.W. Hobbs, T. Diaz de la Rubia, L.E. Rehn, S.J. Zinkle (Eds.), Microstructural Evolution During Irradiation, MRS Symposium Proceedings 439 (Materials Research Society, Pittsburgh, 1997).
[28] C.L. Liu, G.R. Odette, B.D. Wirth, G.E. Lucas, A LMC simulation of nanophase structures in irradiated pressure vessel Cu–Ni–Mn–Si steels, Mater. Sci. Eng. A, in press.
[29] G.R. Odette, G.E. Lucas, D.K. Klingensmith, Anomalous hardening in model alloys and steels thermally aged at 290°C and 350°C: Implications to low flux irradiation embrittlement, in: R.K. Nanstad, M.L. Hamilton, F.A. Garner, A.S. Kumar (Eds.), Effects of Irradiation on Materials: 18th Int. Symp., ASTM STP 1325 (American Society for Testing and Materials, West Conshohoken, PA) accepted.
[30] G.R. Odette, G.E. Lucas, D. Klingensmith, Irradiation hardening of pressure vessel steels at 60°C: The role of thermal neutrons and boron, in: R.K. Nanstad, M.L. Hamilton, F.A. Garner, A.S. Kumar (Eds.), Effects of Irradiation on Materials: 18th Int. Symp., ASTM STP 1325 (American Society for Testing and Materials, West Conshohoken, PA) accepted.
[31] D.E. Alexander, L.E. Rehn, K. Farrell, R.E. Stoller, J. Nucl. Mater. 228 (1996) 68.
[32] G.R. Odette, C.K. Sheeks, in: J.R. Holland, L.K. Mansur, D.I. Potter (Eds.), Phase Stability During Irradiation (The Metallurgical Society, Warrendale, PA, 1981) p. 415.
[33] A.D. le Claire, Philos. Mag. 172 (1970) 819.
[34] M.W. Finnis, J.E. Sinclair, Philos. Mag. A50 (1984) 45.
[35] A.F. Calder, D.J. Bacon, J. Nucl. Mater. 207 (1993) 25.
[36] G.J. Ackland, G.I. Tichy, V. Vitek, M.W. Finnis, Philos. Mag. A56 (1987) 735.
[37] B.D. Wirth, G.R. Odette, unpublished research.
[38] G.J. Ackland, V. Vitek, Phys. Rev. B41 (1990) 10324.